

Contact angle hysteresis effects on a drop sitting on an incline plane

Pablo D. Ravazzoli, Ingrith Cuellar, Alejandro G. González and Javier A. Diez
*Instituto de Física Arroyo Seco, Universidad Nacional del Centro de la Provincia de Buenos Aires,
and CIFICEN-CONICET-CICPBA, Pinto 399, 7000, Tandil, Argentina*

We study the contact angle hysteresis and morphology changes of a liquid drop sitting on a solid substrate inclined with respect to the horizontal at an angle α . This one is always smaller than the critical one, α_{crit} , above which the drop would start to slide down. The hysteresis cycle is performed for positive and negative α 's ($|\alpha| < \alpha_{crit}$), and a complete study of the changes in contact angles, free surface and footprint shape is carried out. The drop shape is analyzed in terms of a solution of the equilibrium pressure equation within and out of the long-wave model (lubrication approximation). Within this approximation, we obtain a truncated analytical solution that describes the static drop shapes, that is successfully compared with experimental data. This solution is of practical interest since it allows for a complete description of all the drop features, such as its footprint shape or contact angle distribution around the drop periphery, starting from a very small set of relatively easy to measure drop parameters.

I. INTRODUCTION

The problem of a sessile drop sitting on an incline has been the subject of numerous investigations in the last three decades. Some of them have been concerned with the relationship between the maximum plane inclination above which the drop slides down, α_{crit} , and the parameters characterizing the initial conditions [1–4]. Many studies aim to describe the retention forces needed to achieve this critical inclination angle [5–9], while other related works focus on the dynamics of droplets sliding down an incline [10, 11].

An aspect that has drawn considerable attention in this context is the shape that a tilted sessile drop adopts under different plane inclinations, α (see Fig. 1). This problem can be theoretically tackled by means of two equivalent approaches, namely, the equilibrium of pressures (by using the Young–Laplace equation) or the energy minimization method (by considering both surface and gravitational energies in an Euler–Lagrange framework). The latter has been considered by using different assumptions, for example, that footprints remains circular $\alpha \neq 0$ [12–15]. However, there is experimental evidence that the footprints of drops on inclines are not circular. Therefore, some authors have proposed alternative non-circular footprints, such as straight lines and circular endings [1]. Although this shape is very simple, and easy to deal with, it does not correspond to observations. A more accurate approximation was developed in [16], where the drop footprint is approximated by two superimposed ellipses sharing a common tangent at the maximum width. However, these proposals are ad-hoc and are not based on physical grounds.

The use of the Surface Evolver simulation tool [4, 17–19] is able to yield other non-circular footprints. Alternative approaches numerically obtain the footprint shapes considering an hybrid diffuse interface with smoothed particle hydrodynamics model [20], or an equilibrium variation approach which accounts for a drop's virtual motion on the footprint [21]. The experiments in [22] for a tilted water drop on a siliconized flat glass slide have shown that there are three transitions of partial depinning, namely: that of the advancing and receding parts of the contact line, and that of the entire contact line leading to the drops translational motion. However, as we will see here, the first two stages do not necessarily occur successively as α increases, but an important overlapping of both stages is possible. Chou et al. [17] have compared their theory with the experimental footprints from [22], and the discrepancies were attributed to the initially non-circular footprint of the experiments. In this work, we will observe that the experiments carried out in [17] correspond only to the initial stages of the complete α -cycles reported here.

The analysis of this deceitfully simple problem is very complex since it requires a thorough comprehension of the phenomena related to contact angle hysteresis. In general, this property has been studied by measuring the contact angle of a sessile drop on a horizontal plane for a given volume, V . This is usually done by injecting and withdrawing liquid with a needle touching the top of the drop (see e.g. [23]). A recent study [24] has shown that, under volume changes, the drop achieves its equilibrium by adjusting the contact angle, θ , within a given interval with three different contact line behaviors, namely: it remains pinned, or it alternatively depins and reaches equilibrium after having receded or advanced. This cycle is depicted in Fig. 2, where Δr indicates the displacement of the equilibrium contact line from the initial situation, marked by the point O where $\Delta r = 0$ (see also Fig. 2b in [24]). The entrance to the cycle is shown by the path OA along which the drop volume increases while θ remains constant. The right (AB) and bottom (BC) branches result from decreasing volumes ($\Delta V < 0$), while the left (CD) and top (DA) ones correspond to $\Delta V > 0$. The three possible behaviors mentioned above are limited by four characteristic contact angles, which define the following three stages: (i) the contact line remains pinned for $\theta_{rcd} < \theta < \theta_{adv}$, (ii) it recedes and reaches equilibrium for $\theta_{min} < \theta < \theta_{rcd}$, and (iii) it advances and reaches equilibrium for $\theta_{adv} < \theta < \theta_{max}$.

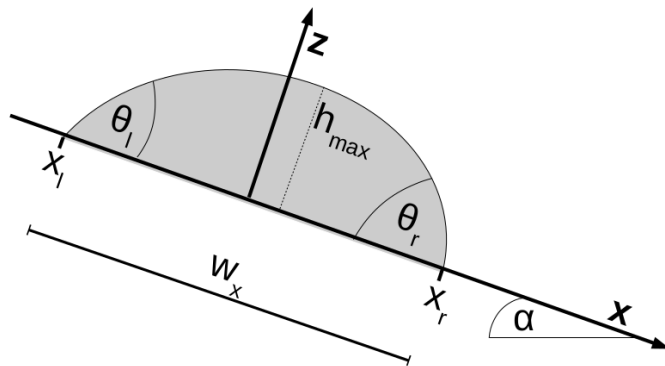


FIG. 1: Sketch of the drop cross section along the symmetry vertical plane on an incline.

Note that it is usual to define the hysteresis range only by the interval of case (i), where the contact line is pinned. However, other equilibrium solutions are also found out of this range after some contact line displacements, and they exist within the wider interval $(\theta_{min}, \theta_{max})$.

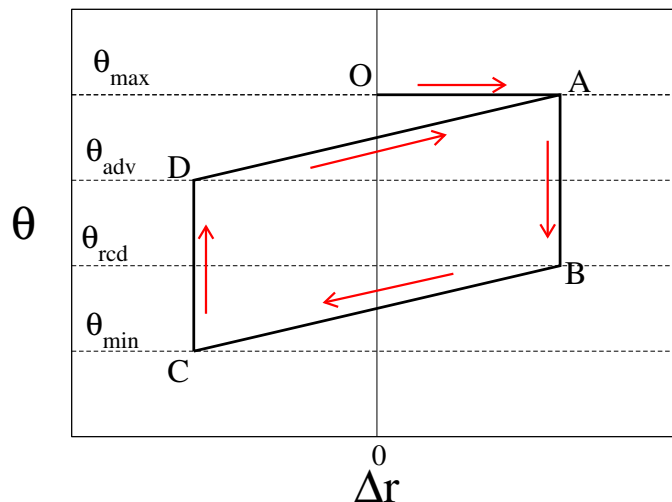


FIG. 2: Scheme of the contact angle hysteresis cycle. Point O corresponds to the initial situation where drop volume is V and $\Delta r = 0$. The line OA shows the path to enter the cycle ABCD. Both V and θ decrease (increase) from A to C (C to A). Note that there is a pinned contact line ($\Delta r = const.$) along AB and CD, while there is depinning along BC and DA (see Fig. 2b in [24]).

In this paper, instead of considering the drop volume, V , as the variable parameter for $\alpha = 0$, we vary the inclination angle, α , for given V . The goal is to show that a similar hysteresis cycle with the same four characteristic angles can be found by means of this alternative procedure. Thus, we wish to confirm that the hysteresis cycle is an intrinsic property of the liquid–solid interaction, no matter which parameter is varied around it, V or α . In particular, we will start the cycle at $\alpha = 0$ and analyze the drop equilibrium states within the interval $(-\alpha_{max}, \alpha_{max})$, where $\alpha_{max} \lesssim \alpha_{crit}$ (in our case $\alpha_{crit} \approx 26^\circ$). One advantage of the procedure of changing α for fixed V is that it is not invasive, since the drop is only in contact with the substrate, and no needle is perturbing its free surface. On the other hand, the axial symmetry of the procedure with variable V and $\alpha = 0^\circ$ is lost, since the drop footprint is no longer circular as the plane is inclined. This seeming drawback is here utilized to obtain two hysteresis cycles, one for the left and another for right contact points of the drop when observed laterally. Note that these points change their downhill or uphill character as α changes sign.

Moreover, we are also concerned with the modifications of the drop shape as the inclination varies in the interval $(-\alpha_{max}, \alpha_{max})$. In particular, the experiments show an expected symmetry of the profiles for positive and negative values of α , which can be used as an assessment of the experimental accuracy. We also calculate the theoretical drop shape

by numerically solving the pressure equilibrium equation for the drop thickness, h . The accuracy of the long-wave theory approach is discussed by numerically solving the simplified equation for h . Within this approximation, known as lubrication theory, we find an analytical solution in the form of a series. In order to obtain a solution for practical use, we propose a truncated expression, whose coefficients can be calculated from a small set of easily measured drop parameters, namely, the drop extensions along both downhill and transverse directions, and the downhill contact angle. Using this model, we are able to predict other measured features of the drop that require more complex diagnostics, such as the uphill contact angle, the maximum drop thickness, and the footprint shape. A comparison is made between these predictions and their measured counterparts.

The paper is organized as follows. Section II describes the experimental setup and presents measured data regarding the whole hysteresis cycle, which can be divided into five main branches. We also analyze the drop thickness profiles by comparing measurements for positive and negative α 's. Then, we describe the formalism and different approaches to account for the calculation of the equilibrium drop shape in Section III. The numerical solutions for the approaches with and without lubrication approximation are compared with the experimental data in Section IV. A similar comparison is done in Section V for the truncated solution under the long-wave approximation. Finally, Section VI is devoted to a summary and conclusions.

II. EXPERIMENTS AND DESCRIPTION OF THE HYSTERESIS CYCLE

The experiments are performed on a substrate which is partially wetted by our working fluid, namely a silicone oil (polydimethylsiloxane, PDMS). The substrate is a glass (microscope slide) coated with a fluorinated solution (EGC-1700 of 3M) by controlling both the dip coating velocity (≈ 0.1 cm/min) and the drying time of the solvent solution ($t \approx 30$ min) in an oven at temperature $T \approx 40^\circ\text{C}$. Under this protocol we ensure that the PDMS partially wets the substrate in a repeatable way, so that a drop of given volume placed on a horizontal substrate always reaches the same contact angle (within the experimental error, $\pm 0.5^\circ$). Surface tension, γ , and density, ρ , of PDMS are measured with a Krüss K11 tensiometer, while its viscosity, μ , is determined with a Haake VT550 rotating viscometer. The values of these parameters are: $\gamma = 21$ dyn/cm, $\rho = 0.97$ g/cm³, and $\mu = 21.7$ Poise at temperature $T = 20^\circ\text{C}$.

The same kind of substrate and PDMS was previously used in [24], where the static contact angle, θ , of a single sessile drop with circular footprint on a horizontal substrate was measured. In that work, we were able to study the hysteresis cycle of θ by injecting and withdrawing fluid with a needle in contact with the top of the drop. This was done by measuring θ (as well as the thickness profile, $h(x)$) with a Rame-Hart Model 250 goniometer. In particular, we found $\theta_{max} = 55^\circ$ and $\theta_{min} = 40^\circ$, while the contact angles at which the contact line displaces to achieve equilibrium, that is the advancing and receding angles, were $\theta_{adv} = 52^\circ$ and $\theta_{rcd} = 46^\circ$, respectively.

Unlike the experiments in [24], the goniometer is now mounted on a tilted base with a variable inclination angle, α . Since the goal here is to analyze the deformations of the drop shape due to changes in α , the substrate is inclined in successive steps of $\Delta\alpha = 2.5^\circ$, and the cycle $0^\circ \rightarrow \alpha_{max} \rightarrow 0^\circ \rightarrow -\alpha_{max} \rightarrow 0^\circ \rightarrow \alpha_{max}$, with $\alpha_{max} < \alpha_{crit} \approx 26^\circ$ is considered (see Fig. 3) where the branches are numbered from 1 to 5, the starting point is denoted by O, and the extreme points by A, B, C, D and E. We measure the positions of the contact line points on the right, x_r , and left, x_l , of the drop profile at the xz -plane (see Fig. 1) as well as the corresponding contact angles, θ_r and θ_l . Note that x_r corresponds to the downhill (uphill) point for $\alpha > 0$ ($\alpha < 0$), and vice versa for x_l .

The thickness profiles and footprint shapes at every point of the cycle are obtained from images such as those shown in Fig. 4. The top (bottom) line shows the side (top) views of the drop for $\alpha = 0^\circ, 12.5^\circ$, and 25° . The reflected image of the drop on the substrate, as seen at the top line of the pictures, is used to determine the substrate position as well as the segment connecting the side vertices (its length yields the drop extension, w_x). The thick green lines in the top line pictures indicate the thickness profiles, while those in the top views (bottom line) correspond to the footprint shapes.

The initial contact angle at point O, θ_0 , depends on how the drop is set up on the substrate. For this task, we use an automatic dispenser syringe; thus, θ_0 may result in the range $\theta_{adv} < \theta_0 < \theta_{max}$ since the drop reaches equilibrium by spreading after being deposited with the needle. Usually, it results $\theta_0 = \theta_{max}$, but it can be reduced a bit if some drop fluid is withdrawn with the needle. In the following, we will analyze the effects of both α_{max} and θ_0 on the hysteresis cycle.

We start our study with $\alpha_{max} = 25^\circ$ and $\theta_0 = \theta_{max} = 55^\circ$. The measured displacements Δx_l and Δx_r (with respect to their positions for $\alpha = 0^\circ$) versus α are shown in Fig. 5a by squares and circles, respectively. The accuracy of these displacements is of ± 1 pixel which, according to our optical magnification, corresponds to $\pm 11\mu\text{m}$. The main α -sequence represented in Fig. 3 yields the cycles ABCDE for both Δx_l (full red squares) and Δx_r (full blue circles) as shown in Fig. 5a. The entry paths, OA, to the cycles are shown by hollow black squares and circles, respectively. Analogous considerations apply for θ_l and θ_r in Fig. 5b. Note that only the path OA is similar to the experiments reported in Section 3.B of [17], where no detailed description of the footprints shape was provided.

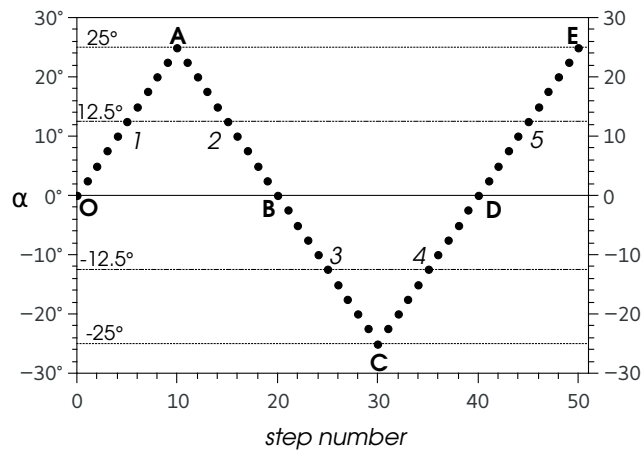


FIG. 3: Inclination angle, α , as a function of the number of steps for $\alpha_{max} = 25^\circ$. The complete cycle is: $0^\circ \rightarrow 25^\circ \rightarrow 0^\circ \rightarrow -25^\circ \rightarrow 0^\circ \rightarrow 25^\circ$. Each step corresponds to $\Delta\alpha = 2.5^\circ$. The numbers and letters indicate the branches and their extreme points, respectively.

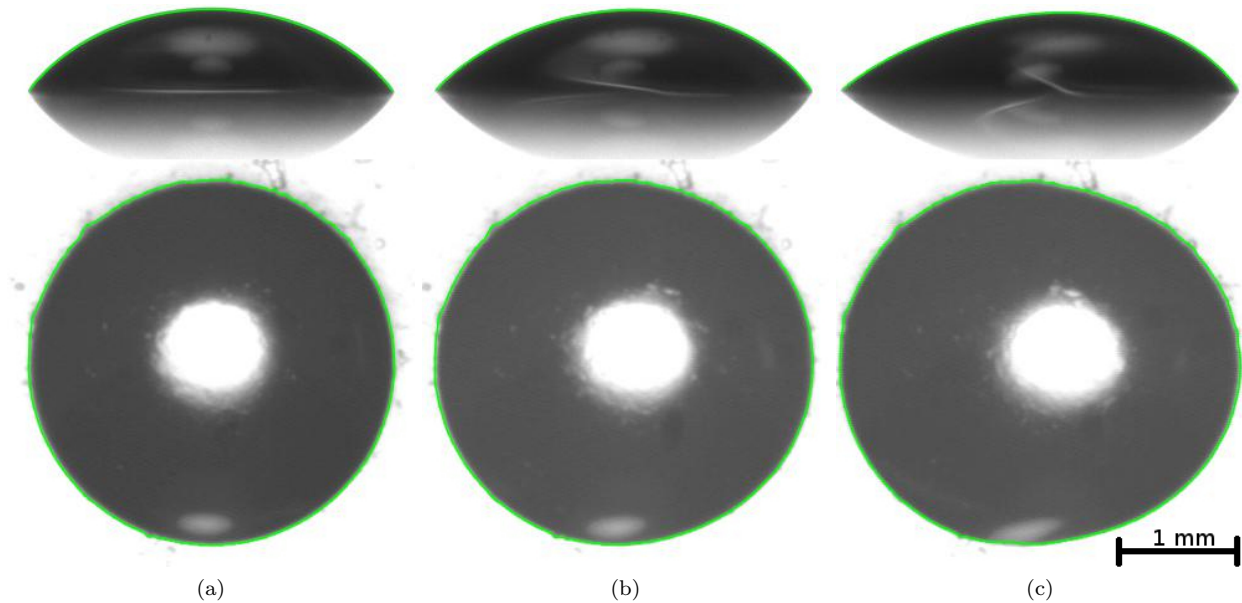


FIG. 4: Images as obtained from the goniometer of the side (top line) and top (bottom line) views of the drop for three inclination angles, α . (a) $\alpha = 0^\circ$, (b) $\alpha = 12.5^\circ$, and (c) $\alpha = 25^\circ$. The green lines are the contours extracted from the image analysis. The bar in (c) gives the scale of all pictures.

Consequently, by considering α as a varying parameter, we are able to construct the contact angle hysteresis cycles, as shown in Fig. 6. Clearly, this cycle has properties similar to those described for the one depicted in Fig. 2, which uses the drop volume V as a varying parameter. Moreover, the values of the angles limiting the pinning and depinning regions are coincident with those in [24], where the same kind of substrate and fluid were used.

Equivalent cycles are also obtained for smaller $\theta_0 = 48^\circ$ and same α_{max} than in Fig. 6, i.e. for $\theta_0 < \theta_{adv}$ (see Fig. 7a). The Δx -range of the cycles decreases significantly (from ≈ 0.06 cm to ≈ 0.01 cm), but the θ -range is only slightly smaller and scarcely out of the pinning interval $(\theta_{rcd}, \theta_{adv})$. This is because the equilibrium drop states along the OA branch can be reached just by increasing (decreasing) θ_r (θ_l) as α increases without need to displace the contact line. These behaviors are similar to those shown in Section 3.C of [17]. In fact, the displacements occur after θ_r (θ_l) has approached to θ_{adv} (θ_{rcd}), i.e. when the contact angles reach the boundaries of the pinning interval $(\theta_{rcd}, \theta_{adv})$. This description, based on θ versus Δx , is quite general and has the advantage that it avoids the dependence on α ,

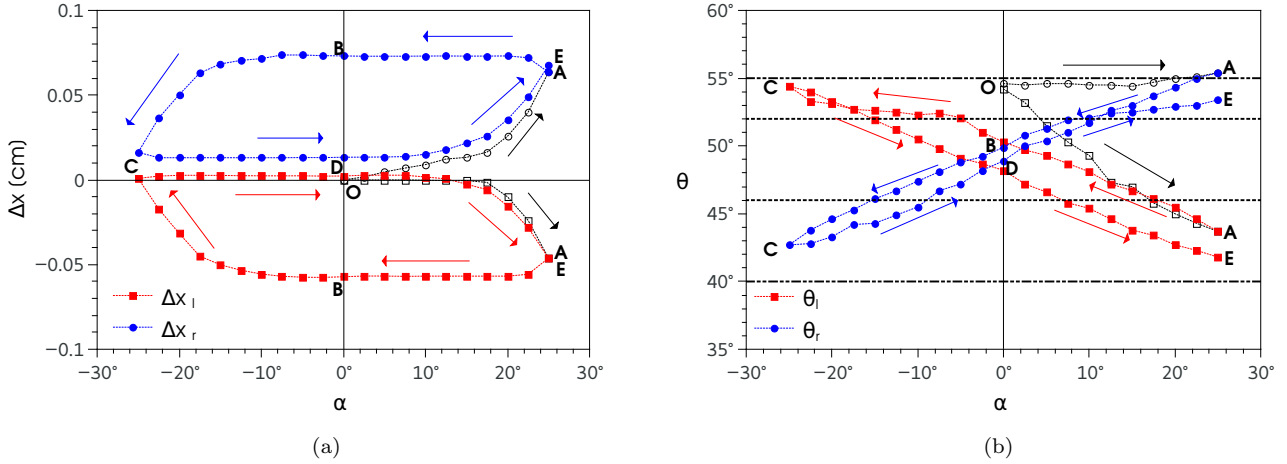


FIG. 5: Maximum plane inclination $\alpha_{max} = 25^\circ$ and initial contact angle $\theta_0 = 55^\circ$: (a) Contact lines displacements Δx_l and Δx_r (with respect to their positions at $\alpha = 0^\circ$) versus α . (b) Contact angles θ_l and θ_r versus α . The horizontal dotted (dot-dashed) lines in (b) correspond to $\theta_{rcd} = 46^\circ$ and $\theta_{adv} = 52^\circ$ ($\theta_{min} = 40^\circ$ and $\theta_{max} = 55^\circ$). The drop volume is $V = 0.657a^3 = 2.17 \text{ mm}^3$.

in contrast to the experimental results analysis performed in [4]. Note that the value of α at which θ_r reaches θ_{adv} (namely, α_m in [4]) is not independent of θ_0 . Moreover, the numerical results in [18] show that α_1 ($= \alpha_m$ in [4]) depends not only on θ_0 but also on the drop volume, V . On the other hand, the results in Figs. 6 and 7 show that the transitions regions in the hysteresis cycle are intrinsic properties of the system, and therefore independent of both θ_0 and V .

In Fig. 7b, we keep the same initial condition as in Fig. 6 and reduce the value of α_{max} to 15° . We observe that $\Delta x_r > 0$ only along the initial branch OA, while the cycles show variations of both θ_r and θ_l with $\Delta x_r = \Delta x_l = 0$, i.e. with pinned contact lines. The reason for this behavior is that for such small α , the equilibrium states can be reached for θ_r and θ_l greater than θ_{rcd} , without need to displace the contact lines.

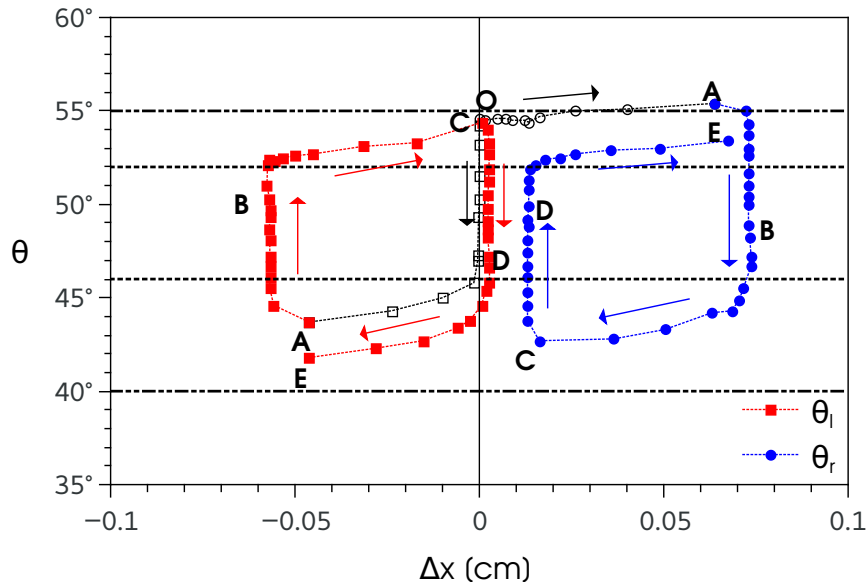


FIG. 6: Contact angles, θ_l and θ_r , versus contact line displacements, Δx_l and Δx_r , for $\alpha_{max} = 25^\circ$ and $\theta_0 = 55^\circ$ for the drop in Fig. 5. The horizontal dotted (dot-dashed) lines correspond to $\theta_{rcd} = 46^\circ$ and $\theta_{adv} = 52^\circ$ ($\theta_{min} = 40^\circ$ and $\theta_{max} = 55^\circ$).

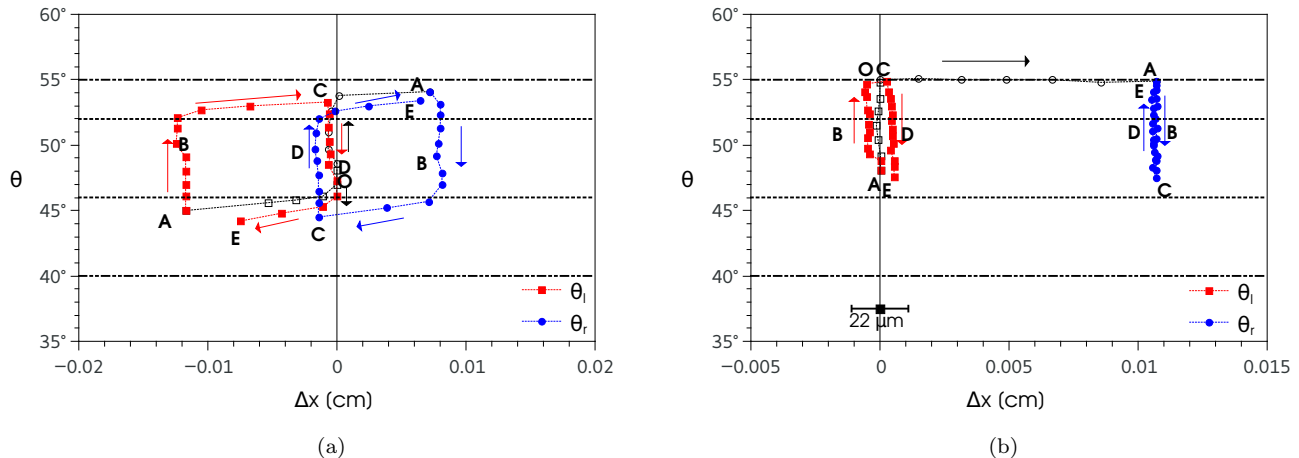


FIG. 7: Contact angles, θ_l and θ_r , versus contact line displacements, Δx_l and Δx_r , for: (a) $\alpha_{max} = 25^\circ$ and $\theta_0 = 48^\circ$ ($V = 0.474a^3 = 1.57 \text{ mm}^3$). (b) $\alpha_{max} = 15^\circ$ and $\theta_0 = 55^\circ$ ($V = 0.519a^3 = 1.72 \text{ mm}^3$). The horizontal segment in (b) corresponds to the error bar for Δx .

A. Branch 1: From $\alpha = 0$ to $\alpha = 25^\circ$ (O \rightarrow A with $\alpha_{max} = 25^\circ$ and $\theta_0 = 55^\circ$)

As α increases from 0 to 25° we observe that the downhill contact point, x_r , displaces downwards a bit more than the uphill one, x_l (see Fig. 5a, O \rightarrow A for both Δx 's). Concomitantly, the downhill contact angle approaches θ_{max} and remains practically constant until point A (see Fig. 5b), while the uphill contact angle, θ_l , significantly diminishes, surpassing θ_{red} and approaching θ_{min} (see Fig. 5b). These facts indicate that $\alpha = 25^\circ$ is very close to the limiting angle, α_{crit} , beyond which the drop would not remain at rest and would slide down the plane instead.

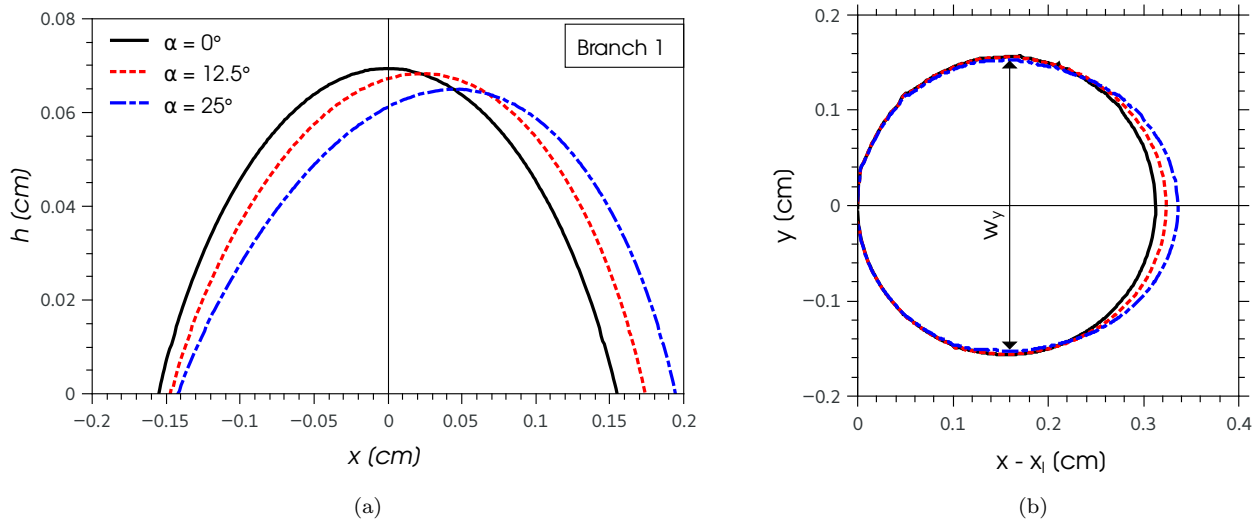


FIG. 8: Branch 1: (a) Thickness profiles at $\alpha = 0^\circ$ (solid lines), 12.5° (dashed lines), and 25° (dot-dashed line). (b) Corresponding footprints shifted so that the most left points are coincident. The drop volume is $V = 0.876a^3 = 2.9 \text{ mm}^3$

The experimental thickness profiles shown in Fig. 8a indicate that the drop width, w_x , increases while the maximum thickness decreases as the plane becomes more inclined. The footprints at points O, A and an intermediate point $\alpha = 12.5^\circ$ are displaced to coincide at their most left point and compared in Fig. 8b. Note that the footprints are distorted from a circular shape only in the frontal part, i.e. for $x > w_x/2$, where they become more elongated. Interestingly, the maximum transversal width of the footprints, w_y , remains constant for all α 's.

Our experimental data for this branch can be compared with those reported in the literature. In order to do that,

we parameterize the effects of the component of gravity along the plane by defining the Bond number as

$$Bo = \frac{w_x^2}{a^2} \sin \alpha, \quad (1)$$

where $a = \sqrt{\gamma/(\rho g)}$ is the capillary distance. Note that w_x is also a function of α (see Fig. 8b). For instance, Fig. 9a shows that the ratio θ_r/θ_{max} (diamonds) remains very close to unity as the plane is inclined. This result is in agreement with previously reported experimental [22, 25] and numerical [17] results. Analogously to what was done in [25], we plot θ_l versus Bo by considering its relative deviation from θ_{min} as $\Theta = (\theta_l - \theta_{min})/(\theta_{max} - \theta_{min})$. Similarly to what was reported in [25], we also find a linear dependence for this relationship. Slopes differences are a consequence of dealing with different liquid–substrate combinations. In Fig. 9b we show the ratio θ_l/θ_r versus Bo and obtain a quadratic fitting function (thick solid line). Interestingly, this curve is similar to that reported in [25] for other combinations of liquids and surfaces (see dashed line and formulae in the figure).

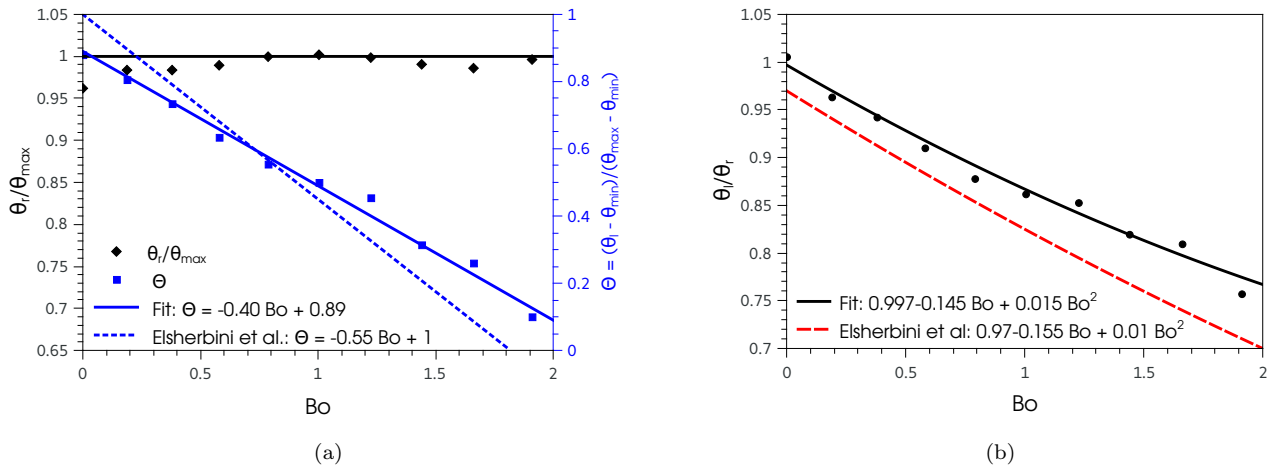


FIG. 9: Contact angles as functions of Bond number, Bo , along Branch 1: (a) θ_r/θ_{max} (diamonds) and the relative deviation of θ_l : $\Theta = (\theta_l - \theta_{min})/(\theta_{max} - \theta_{min})$ (squares). The thick solid line is the best quadratic fit of the squares. (b) Experimental data and best quadratic fit for ratio of both contact angles θ_l/θ_r . The dashed line corresponds to [25].

B. Branches 2, 3 and 4

As the plane is reverted to the horizontal position, the drop does not recover the same shapes for a given α in different branches due to the hysteresis of the contact angle. For instance, for $\alpha = 12.5^\circ$ only the position x_l is almost coincident when comparing branches 1 and 2, but all other parameters differ. The effects for the thickness profiles and footprints with the same α are shown in Fig. 10.

We also verify that the profiles as well as the footprints depend not only on α but also on the direction in which α is changing, i.e. whether it is increasing or decreasing. In fact, we compare the profiles for $\alpha = 12.5^\circ$ for branches 1 ($\alpha > 0$) and 3 ($\alpha < 0$) coincide when $|\alpha|$ is increasing. The profiles for branches 2 ($\alpha > 0$) and 4 ($\alpha < 0$) are identical when $|\alpha|$ is decreasing. This confirms the fact that (as expected) the sign of α is irrelevant.

Fig 11a compares the profiles for $\alpha = 0$ at points O, B and D, where the drop has been affected by both positive and negative inclination angles. Clearly, the profile at B and D do not coincide with that at O, but those at B and D are coincident if they are shifted to the left and right, respectively, till both maximums are at $x = 0$. This fact implies that the effect of changing the sign of α only has the effect of exchanging the roles of the points x_l and x_r , which is an expected result. Therefore, this experimental verification reinforces the confidence in the accuracy of our measurements.

When we consider the area of the thickness profile, \mathcal{A} , all along the cycle, we find that it remains practically constant with a value $\mathcal{A} = (0.694 \pm 0.007)a^2$. This allows us to compare this result with the predictions for a two dimensional drop [7], i.e. for the problem of an infinitely long filament placed transversal to the incline. For instance, in [26] we find the following relationship between \mathcal{A} and the contact angles,

$$2 \tan \delta \tan \theta_0 = \frac{\mathcal{A}}{a^2} \sin \alpha \quad (2)$$

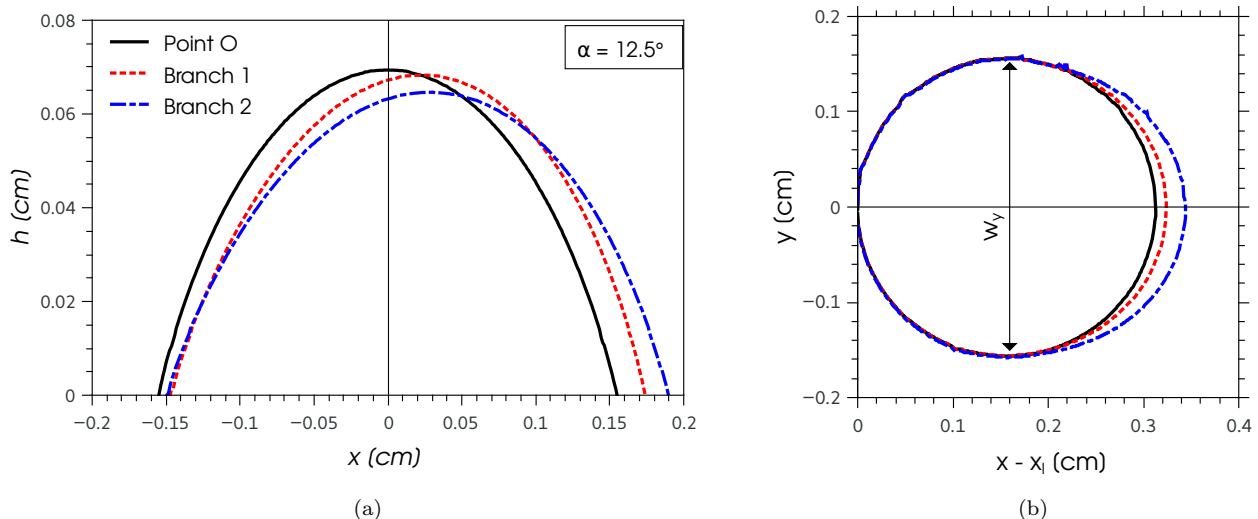


FIG. 10: Thickness profiles for $\alpha = 12.5^\circ$ at branch 1 (dashed line) and branch 2 (dot-dashed lines). The solid line corresponds to point O at $\alpha = 0$ and it is shown for comparison. (b) Corresponding footprints shifted so that the most left points are coincident.

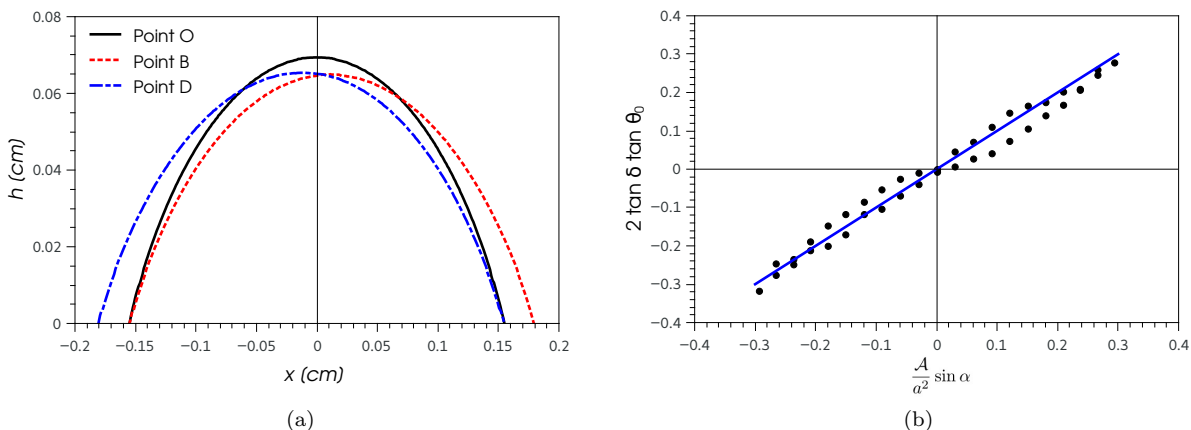


FIG. 11: (a) Thickness profiles for $\alpha = 0^\circ$ at different extreme points of the cycle: Solid line at start (point O), dashed line at the end of branch 2 (point B), and dot-dashed line at the end of branch 4 (point D). (b) Experimental data plotted in terms of the left and right hand sides of Eq. (2) compared with the identity line.) Note that the profiles are practically coincident, if they are shifted towards left and right, respectively, till both maximums are at $x = 0$.

where $\delta = (\theta_r - \theta_l)/2$ and $\theta_0 = (\theta_r + \theta_l)/2$. In order to compare this prediction with the present experiments, we plot the l.h.s of Eq. (2) as obtained from the measured contact angles versus its r.h.s. considering the measured values of \mathcal{A} (see symbols in Fig. 11b). The good agreement with the line with the identity line (representing Eq. (2)) shows that this formulation is still valid for three dimensional drops as those studied in this work.

III. DROP SHAPE

One main observation of the experiments reported in Section II, as well as in the literature (see e.g. [1, 3, 5]), is that the shape of the footprint does not remain circular for $\alpha > 0$. However, since most of the analytical approaches restrict to small values of α , those studies have considered a circular shape for the footprint [15, 25]. Instead, we will extend now our previous theory in [27] for non-circular footprints on horizontal planes to inclined ones. In particular, we will adapt that formalism in polar coordinates to the present case.

The governing equation for the thickness profile of the static drop can be obtained by considering the balance

between the capillary pressure and both components of the gravitational force. In dimensionless form, we have

$$-\kappa + h \cos \alpha - x \sin \alpha = P = \text{const.}, \quad (3)$$

where the thickness $h(x, y)$ and the spatial coordinates (x, y) are in units of a , and P is the drop pressure in units of γ/a . Here, $\kappa = \nabla \cdot \mathbf{n}$ is the curvature of the drop free surface with normal vector $\mathbf{n} = \nabla F/|\nabla F|$, where $F = z - h(x, y) = 0$ defines it. Thus, we have

$$-\nabla \cdot \left(\frac{\nabla h}{\sqrt{1 + \epsilon |\nabla h|^2}} \right) + h \cos \alpha - x \sin \alpha = P = \text{const.}, \quad (4)$$

For $\epsilon = 1$, the first term stands for the full surface curvature, while for $\epsilon = 0$ it yields the curvature only valid for small free surface slopes, i.e. $|\nabla h|^2 \ll 1$, in the context of the long-wave theory (lubrication approximation). The solution domain is the drop footprint, whose border line is denoted by a closed curve $\Gamma_\alpha(x, y) = 0$ where $h = 0$ for a given α . The determination of the constant P and the footprint shape, $\Gamma_\alpha(x, y) = 0$, depends on the approach used to solve Eq. (4) (see Sections IV and V).

A first approach to simplify this equation consists on assuming the validity of the lubrication approximation, even if the drops considered here do not have small contact angles. Thus, Eq. (4) with $\epsilon = 0$ reads as (see e.g. [26])

$$-\nabla^2 h + h \cos \alpha - x \sin \alpha = P, \quad (5)$$

which is a linear equation, similar to that one studied in [27]. In fact, its solution can be written in the form

$$h = h_1 + \frac{P}{\cos \alpha} + x \tan \alpha \quad (6)$$

where h_1 satisfies the homogeneous equation

$$\nabla^2 h_1 - h_1 \cos \alpha = 0. \quad (7)$$

In order to obtain h_1 , it is convenient to define the polar coordinates

$$r = \sqrt{x^2 + y^2}, \quad \varphi = \arctan \frac{y}{x}, \quad (8)$$

where x -origin is defined at the x -coordinate of the point on $\Gamma_\alpha(x, y)$ with maximum y . Thus, this point corresponds to $(0, w_y/2)$, where w_y is the drop width in the transverse direction. Within this reference frame, we assume a factorized solution of Eq. (7) as $h_1 = R(r)\Phi(\varphi)$, and find

$$h(r, \varphi) = \frac{P}{\cos \alpha} + r \cos \varphi \tan \alpha + \sum_{m=0}^{\infty} (A_m \cos m\varphi + B_m \sin m\varphi) I_m(r), \quad (9)$$

where $I_m(r)$ is the modified Bessel function of the first kind. In order to have a symmetric solution with respect to the x -axis, we must have $B_m = 0$ for all m , and then the problem reduces to finding the remaining constants A_m . In principle, this could be accomplished by setting $h = 0$ at an infinite number of points along the footprint border, $\Gamma_\alpha(x, y) = 0$. The evaluation of this series should lead to the same free surface shape as the numerical solution of Eq. (5). In Section V, we will develop an approximation of this series to make this solution of practical use.

IV. NUMERICAL APPROACH AND COMPARISON WITH EXPERIMENTS

In this section, we numerically solve Eqs. (4) and (5). The integration domain $\Gamma_\alpha(x, y)$ is obtained by means of an interpolation curve which fits the footprint data from the experiments. The constant P is adjusted to a given drop volume, V , by means of an iterative procedure.

The value of V is that one measured for $\alpha = 0$ from the thickness profile assuming axial symmetry, i.e. a circular footprint. Figure 12 shows a comparison of the longitudinal numerical thickness profiles, $h(x, y = 0)$, with the experimental ones (symbols) for $\alpha = 0^\circ, 12.5^\circ$ and 25° . Clearly, the full equation for $\epsilon = 1$ fits better these profiles than the long-wave approximation for $\epsilon = 0$. Since the three dimensional solutions have the same volume as the experimental drop, compensations of thickness can be seen along other longitudinal or cross sections. For brevity, we do not show here these differences.

The relative error $e_V = \Delta V/V$ can be estimated from the corresponding errors in the measurement of h_{max} and x_r (or x_l) which are 3% and 1%, respectively, so that $e_V = 5\%$. Consequently, the numerical solutions are also affected by e_V , since their predictions (such as thickness, contact angles, etc.) depend on V through the iterative determination of the constant P in Eqs. (4) and (5). We have estimated this propagation in about 3%. Besides, we have also considered the error of $\pm 1^\circ$ in the measurement of α . In Fig. 13a we show the comparison of h_{max} with the experimental data for the whole range of α , along with the corresponding error bars.

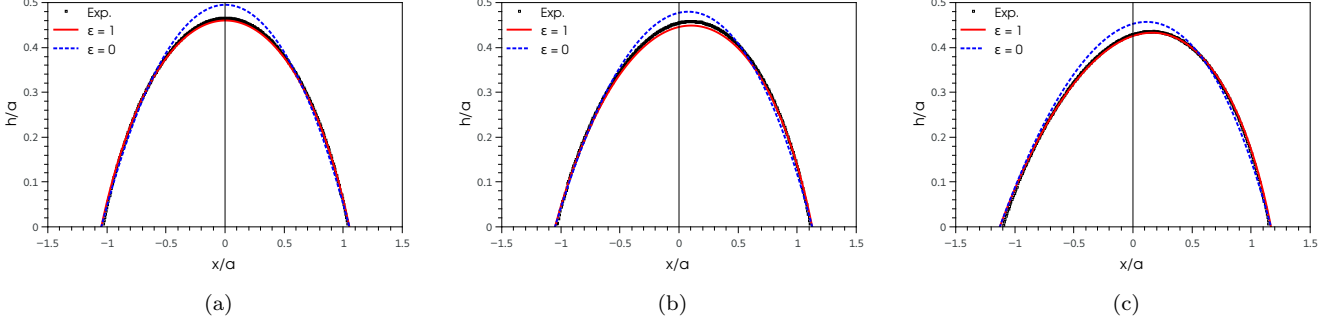


FIG. 12: Comparison between the experimental thickness profile (symbols) and the full ($\epsilon = 1$) and lubrication approximation ($\epsilon = 0$) solutions. (a) $\alpha = 0^\circ$, (b) $\alpha = 12.5^\circ$, and (c) $\alpha = 25^\circ$

Regarding the calculation of the contact angles for the thickness profile $h(x, y = 0)$ at x_l and x_r , we must be careful to use the correct order of approximation for both $\epsilon = 0, 1$. This is because the approximation $\tan \theta \approx \theta$ is used for $\epsilon = 0$, and in general, θ is not so small as to fully satisfy this simplification. Therefore, we write the general formulae,

$$\begin{aligned}\theta(x_r, y = 0) &= -\epsilon \arctan\left(\frac{\partial h}{\partial x}\right) - (1 - \epsilon) \left(\frac{\partial h}{\partial x}\right), \\ \theta(x_l, y = 0) &= \epsilon \arctan\left(\frac{\partial h}{\partial x}\right) + (1 - \epsilon) \left(\frac{\partial h}{\partial x}\right).\end{aligned}\quad (10)$$

Note that $\arctan(\partial h/\partial x) > (\partial h/\partial x)$ for $(\partial h/\partial x) \gtrsim 1$. The comparison with the experimental data is shown in Fig. 13b and c.

In summary, these results allow us to state that the agreement of the numerical solution for $\epsilon = 0$ with the experimental data is marginally within the errors, and that this approximation always yields overestimated values.

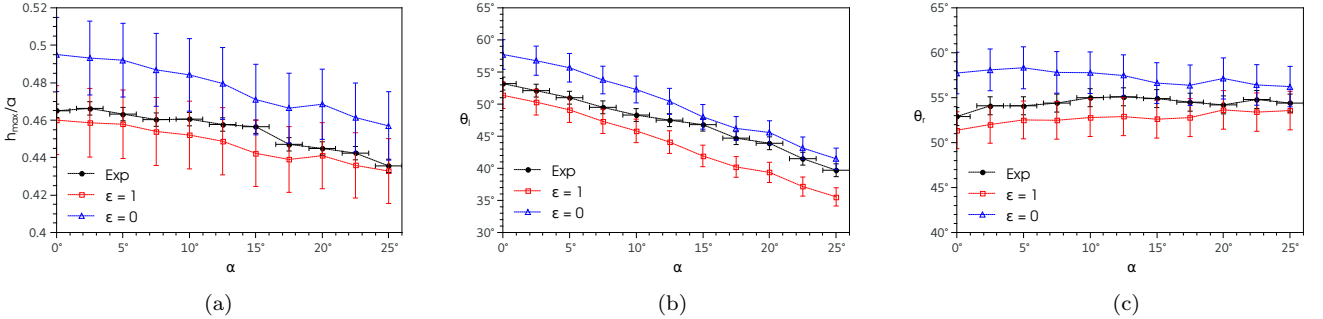


FIG. 13: Comparison between the experimental data and the numerical solutions for $\epsilon = 1$ and $\epsilon = 0$ (Eqs. (4) and (5)) at different inclination angles, α . Both the footprint contour and the drop volume, $V = (0.876 \pm 0.044)a^3 = (2.9 \pm 0.14)mm^3$, are given for each calculation. (a) Maximum thickness of the drop profile, h_{max} . (b) Contact angle at the left side, θ_l . (c) Contact angle at the right side, θ_r .

A. Contact angle distribution along the drop periphery

An important result of the numerical approaches is the contact angle distribution around the drop periphery, i.e the function $\theta(\varphi)$. Except for the work in [25], where θ was measured at eight different azimuthal angles, only the

contact angles at the points $(x_l, 0)$ and $(x_r, 0)$ of the $h(x, 0)$ profile are usually reported in the experiments. The knowledge of this function has been the object of several previous works [15, 25]. Other authors have also performed numerical simulations to obtain $\theta(\varphi)$. Some have assumed a circular shape for the footprint [12, 13] and others have used non-circular shapes obtained by minimization of the required hysteresis range [28]. In general, all the functions $\theta(\varphi)$, except that in [28] which resembles a step function with a linear transition region, show a smooth variation between θ_r and θ_l [11].

The theoretical studies are limited to small Bond numbers, i.e. either small α or small drop diameter, or both (see Eq. (1)). Instead, the two numerical approaches presented here allow to obtain $\theta(\varphi)$ without any restriction on the value of the Bond number.

To do so, we consider the z -component of the normal versor to the free surface, and obtain

$$n_z = \cos \theta(r(\varphi), \varphi) = \left[1 + \left(\frac{\partial h}{\partial r} \right)^2 + \left(\frac{1}{r} \frac{\partial h}{\partial \varphi} \right)^2 \right]^{-1/2}, \quad \epsilon = 1, \quad (11)$$

where $r(\varphi)$ is the footprint boundary given by $\Gamma_\alpha(r, \varphi) = 0$. Within the long-wave approximation, we consider this equation for $\cos \theta \approx 1 - \theta^2/2$, and thus we find

$$\theta(r(\varphi), \varphi) = \pm \sqrt{\left(\frac{\partial h}{\partial r} \right)^2 + \left(\frac{1}{r} \frac{\partial h}{\partial \varphi} \right)^2}, \quad \epsilon = 0. \quad (12)$$

The prediction for $\epsilon = 1$ is compared with the small Bo theory developed by De Coninck et al. [15], which is developed without the lubrication approximation. This solution for $\theta(\varphi)$ is written in the form

$$\cos \theta = (\cos \theta_l - \cos \theta_r) \frac{1 - \cos \varphi}{2} + \cos \theta_r, \quad (13)$$

where θ_r and θ_l are given values. The comparison is done with the values θ_r and θ_l as obtained from the numerical solution for $\epsilon = 1$ at different α 's by using the experimental footprints (see Fig. 14 for $\alpha = 2.5^\circ, 5^\circ, 7.5^\circ$ and 10°). For α as small as 2.5° , the results are in very good agreement with the theory, thus probing that our numerical solution is correct. For larger α 's, we obtain larger values of θ than predicted by Eq. (13), which is only valid for small α 's.

For even larger values of α , we can compare the predictions with $\epsilon = 0$ and 1 between them, as well as with the measured values of θ at the most extreme points, i.e. θ_l and θ_r (see the symbols in Fig. 15a and b for $\alpha = 12.5^\circ$ and 25°). At $\varphi = 0, \pi$, these experimental values are in between the predictions for $\epsilon = 0$ and 1. For $0 < \varphi < \pi$, we observe that for larger α the size of the footprint region facing downhill ($|\varphi| \approx 0$, in which $\theta \approx \theta_r$) increases, and that the transition from θ_l to θ_r becomes more and more abrupt.

V. ANALYTICAL APPROACH AND COMPARISON WITH EXPERIMENTS

In order to look for a useful analytical solution of Eq. (5), we further assume that the shape of the drop can be reasonably estimated by the first three terms of the series in Eq. (9), so that

$$h(r, \varphi) \approx h_{trunc}(r, \varphi) = \frac{P}{\cos \alpha} + r \tan \alpha \cos \varphi + A_0 I_0(r) + A_1 I_1(r) \cos \varphi + A_2 I_2(r) \cos 2\varphi. \quad (14)$$

The advantage of this approach is that the determination of the three constants A_i ($i = 0, 1, 2$) requires to consider only three points at the footprint border, and not the whole footprint as required in the numerical approach. Only an infinite number of points in the footprint could determine all the series coefficients.

Here, we choose the points $(x = x_l, y = 0)$, $(x = x_r, y = 0)$, and $(x = 0, y = w_y/2)$, whose values are given as experimental data. Thus, we write the three conditions in polar coordinates as

$$h_{trunc}(r = r_l, \varphi = \pi) = h_{trunc}(r = r_r, \varphi = 0) = h_{trunc}(r = w_y/2, \varphi = -\pi/2) = 0. \quad (15)$$

where $r_l = -x_l$ and $r_r = x_r$.

The determination of the constant P is done by considering the contact angle at x_r as a known (measured) quantity, i.e. θ_r . Thus, we have the additional condition

$$\theta_r = - \left. \frac{\partial h_{trunc}}{\partial r} \right|_{(r_r, 0)}, \quad (16)$$

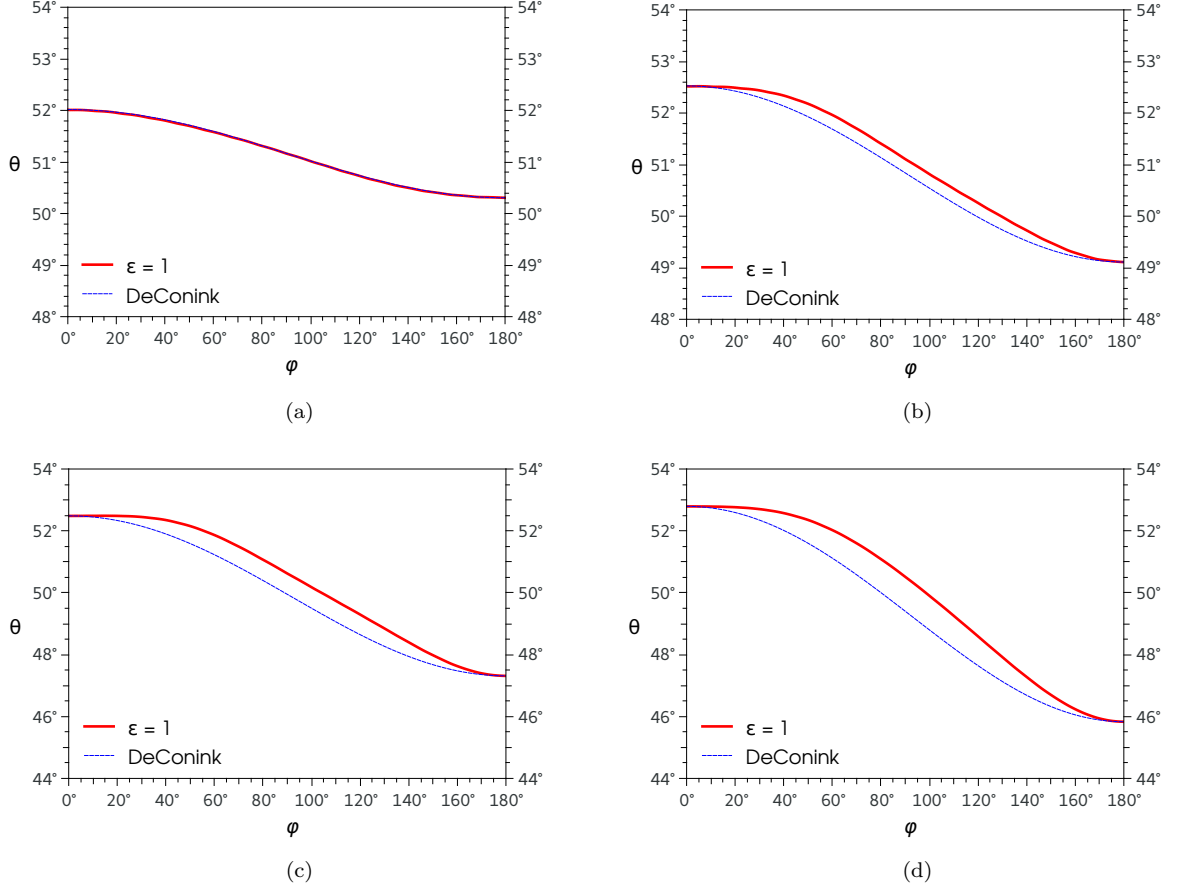


FIG. 14: Azimuthal distribution of contact angle, θ , for various inclination angles, α : (a) $\alpha = 2.5^\circ$ ($Bo = 0.19$, $\theta_r = 52.0^\circ$, $\theta_l = 50.3^\circ$), (b) $\alpha = 5^\circ$ ($Bo = 0.38$, $\theta_r = 52.5^\circ$, $\theta_l = 49.1^\circ$), (c) $\alpha = 7.5^\circ$ ($Bo = 0.58$, $\theta_r = 52.0^\circ$, $\theta_l = 47.3^\circ$), and (d) $\alpha = 10^\circ$ ($Bo = 0.79$, $\theta_r = 52.8^\circ$, $\theta_l = 45.8^\circ$). The values at $\varphi = 0, \pi$ stand for the extreme footprint points facing downslope and upslope, respectively. The thick solid red line corresponds to the solution of Eq. (4). The dashed lines correspond to Eq. (13).

Finally, when all three constants A_i and P have been calculated, the predicted footprint shape is obtained by the implicit equation $h_{trunc}(r, \varphi) = 0$. Figure 16 shows comparisons of footprints (dashed lines) with experimental data (symbols). For both $\alpha = 0^\circ$ and 12.5° , the predicted footprints as given by Eq. (14) are very close to the experimental data within the measurement error. The main difference is observed only on the right side for $\alpha = 25^\circ$. However, we can say that there is a remarkable agreement with the experimental footprints.

The truncated solution also gives predictions for θ_l , h_{max} and V (see Fig. 17). For the contact angle in Fig. 17 we use the expression

$$\theta_l = \left. \frac{\partial h_{trunc}}{\partial r} \right|_{(r_l, \pi)}. \quad (17)$$

Clearly, this solution improves the agreement with the experiments for θ_l and h_{max} respect to the numerical solutions with $\epsilon = 0, 1$ (see Fig. 13a and c). However, the numerical solutions all have the volume V as given by the experiment, while now the predicted volume can have a difference of at most 9% respect to this value (see Fig. 17c). We conjecture that this smaller volume could yield smaller values of both θ_l and h_{max} .

This analytical solution can also yield the azimuthal distribution of contact angle, $\theta(\varphi)$. This is done by plugging Eq. (14) into Eq. (12) with the calculated values of the constants A_i and P . The predicted distributions for $\alpha = 12.5^\circ$ and 25° are shown in Fig. 15 along with the numerical solutions for $\epsilon = 1$ and $\epsilon = 0$. Interestingly, this approximation yields intermediate values of θ for all φ .

In a further attempt to compare our theoretical prediction of $\theta(\varphi)$ with other works, we resort to the fitting cubic

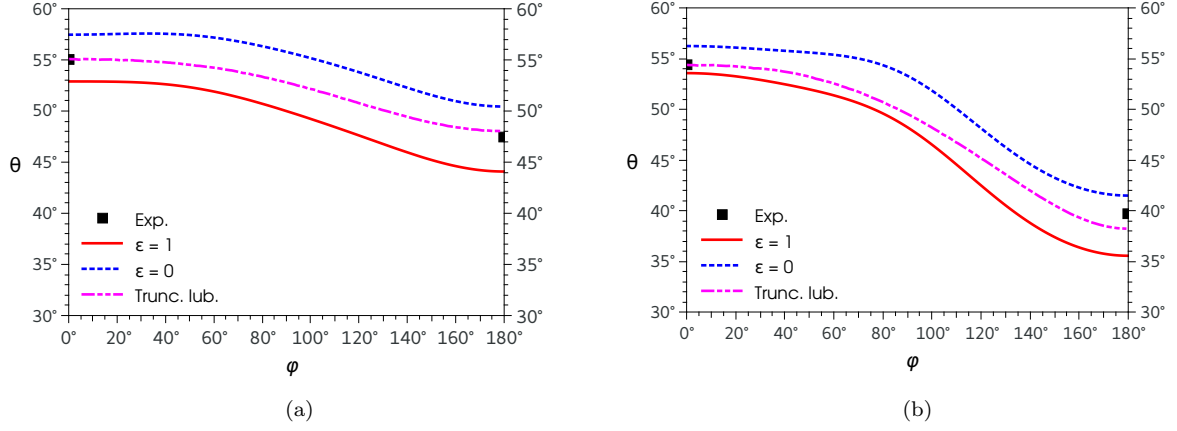


FIG. 15: Comparison between the numerical solutions $\epsilon = 1$ (red solid lines) and $\epsilon = 0$ (blue dashed lines) for the azimuthal distribution of contact angle, θ , for two large values of α . (a) $\alpha = 12.5^\circ$ ($Bo = 1.01$), and (b) $\alpha = 25^\circ$ ($Bo = 2.15$). The (magenta) dot-dashed lines correspond to the truncated analytical solution of the lubrication approximation. The two symbols at $\varphi = 0^\circ$ and 180° stand for the experimental data, namely, θ_l and θ_r .

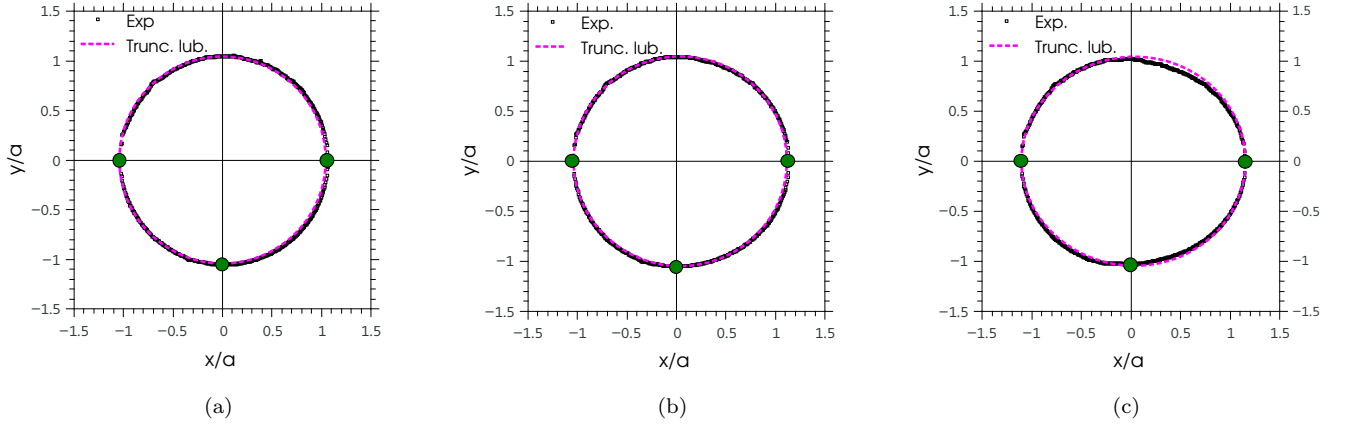


FIG. 16: Comparison between the experimental footprint (symbols) and those predicted by the truncated approximation, Eq. (14) (dashed line), when using only the positions of the three points indicated by the green dots (and the experimental value θ_r) for: (a) $\alpha = 0^\circ$, (b) $\alpha = 12.5^\circ$, and (c) $\alpha = 25^\circ$.

polynomial curve obtained by ElSherbini and Jacobi [25]

$$\theta(\varphi) = (\theta_r - \theta_l) \left(\frac{2\varphi^3}{\pi^3} - \frac{3\varphi^2}{\pi^2} + 1 \right) + \theta_l, \quad (18)$$

where θ_r and θ_l are measured values. According to [25], this expression is valid for $10^\circ < \alpha < 90^\circ$ and $0.75 \text{ mm}^3 < V < 20 \text{ mm}^3$. Fortunately, the values of θ_r and θ_l reported in their Fig. 5a are very close to ours for $\alpha = 25^\circ$. Therefore, we compare in Fig. 18 our solution $\theta(\varphi)$ for the truncated lubrication approximation (see also Fig. 15b) with their experimental data (full circles, whose error bars of $\pm 1.5^\circ$ and $\pm 5^\circ$ in θ and φ are as explained in [25]). Although the available data are limited to a single case ($\alpha = 90^\circ$), we observe that our theory is in good agreement with them. Note that, while theoretical approach requires θ_r and predicts θ_l , Eq. (18) needs an *a priori* knowledge of both values.

VI. SUMMARY AND CONCLUSIONS

In this paper we report novel measurements of the contact angle hysteresis curves and the possible equilibrium states by using the plane inclination, α , up to near a maximum value beyond which the drop starts sliding down.

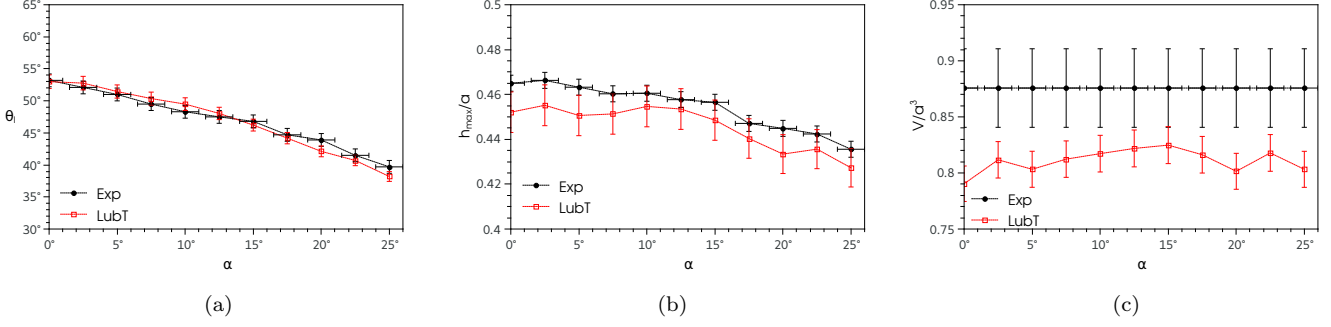


FIG. 17: Comparison between the predictions of h_{trunc} and the experimental data for: (a) the contact angle at the left, b) the maximum drop thickness, and (c) the drop volume.

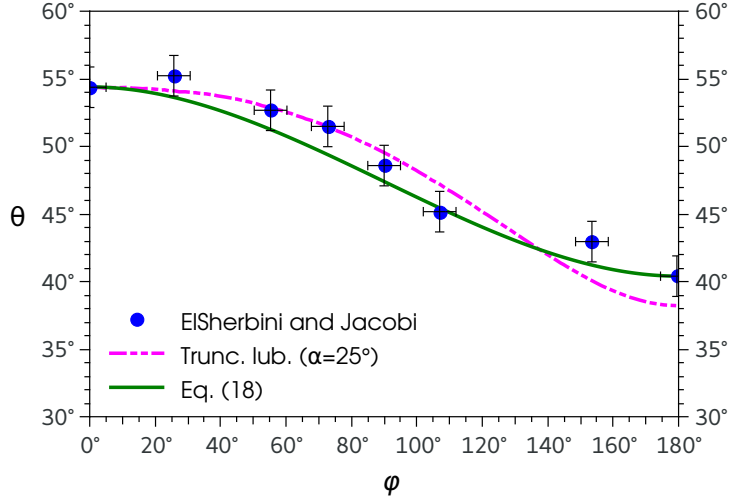


FIG. 18: Comparison between the experimental data of ElSherbini and Jacobi (blue circles with error bars; see Fig. 5a in [25]) with $\theta(\varphi)$ as given by the solution of the truncated lubrication approximation (dashed line; see Fig. 15b). The solid line corresponds to the fitting function given by Eq. (18).

The results are compared with those of usual hysteresis cycles obtained by varying the drop volume, V , instead. The experiments show that both methods yield hysteresis cycles with the same contact angles intervals, a factor confirming that they are an intrinsic consequence of the wetting properties of the system.

While the drop footprint remains circular in the varying volume method, the varying plane inclination method generates equilibrium drops with non-circular footprints. This might seem a drawback of the method at first sight, but provides interesting detailed insight on alternative equilibrium drop shapes that are reached taking into account the hysteresis cycle. In particular, we observe that the most important changes with respect to the initially circular footprint for $\alpha = 0$ occur in the downhill region (see e.g. Fig. 8b). However, these deformations are not the same at different parts of the cycle, even though they correspond to equal α (see Fig. 10b). On the other hand, the present experimental results have been compared successfully with previously reported data (see Fig. 9).

In order to describe the drop shape (both free surface and footprint) at different inclination angles, we have solved the pressure equilibrium equation out of and within the approximation of small contact angles. For this goal, we have resorted to numerical solutions of both the full and approximated equations, as well as to the analytical solution of the latter in the form of a series. The numerical task has shown quantitatively how good are the approximations based on the long-wave theory. As a result, it turns out that they are good enough, since their differences with the measured parameters are within the experimental error interval.

One drawback of these numerical and analytical solutions is that the complete determination of the drop shape requires, for instance, to have measured previously the full shape of the footprint. However, we prove that a truncated expression of the analytical solution suffices to determine both the free surface and the full footprint from a very small set of data at the footprint, namely: the positions of three points on the curve, and a contact angle at one of them.

Our theoretical solution has practical use, since two of those points as well as the contact angle are easily measured from the lateral view of the drop, which is the usual setup in most of the experiments reported in the literature. The third point can be extracted from a knowledge of the transverse width of the drop.

The contact angle variation around the drop periphery, $\theta(\varphi)$, is another important characteristic of the drop shape that can be extracted from the numerical and theoretical analysis presented here. We should note that this angular information is very difficult to measure, specially for an inclined plane. The implementation of a refractive technique similar to that used in [27, 29], which yields θ all along the drop periphery, is left for future work. Up to our knowledge, theoretical models have been developed in the literature only for small inclinations and small drop volumes, when the footprint can be considered circular. We report numerical calculations of $\theta(\varphi)$ without any restriction on α or V , and we also obtain this curve from the theoretical solution with the truncated series. When the former solution is applied by using the measured value of θ_r ($\varphi = 0$), a very good prediction of θ_l ($\varphi = \pi$) is obtained. Unfortunately, comparisons of $\theta(\varphi)$ with experimental data for at other values of φ is not possible, since these measurements have not yet been reported.

In summary, we develop an alternative method to measure the static hysteresis cycle that yields non trivial equilibrium drop shapes, whose main features have been studied here.

Acknowledgments

P. Ravazzoli and I. Cuellar acknowledge postgraduate student fellowships from Consejo Nacional de Investigaciones Científicas y Técnicas (CONICET, Argentina) with Res. 1202/2014 and Res. 4209/2017, respectively. J. Diez and A. González acknowledge support from Agencia Nacional de Promoción Científica y Tecnológica (ANPCyT, Argentina) with Grant No. PICT 1067/2016.

-
- [1] E. B. Dussan V. On the ability of drops or bubbles to stick to non-horizontal surfaces of solids. Part 2: Small drops or bubbles having contact angles of arbitrary size. *J. Fluid Mech.*, 151:1–20, 1985.
 - [2] D. Quéré. Drops at rest on a tilted plane. *Langmuir*, 14:2213–2216, 1998.
 - [3] E. Pierce, F.J. Carmona, and A. Amirfazli. Understanding of sliding and contact angle results in tilted plate experiments. *Colloids and Surfaces A*, 323:73–82, 2008.
 - [4] N. Janardan and M. V. Panchagnula. Effect of the initial conditions on the onset of motion in sessile drops on tilted plates. *Colloids and Surfaces A*, 456:238–245, 2014.
 - [5] C. W. Extrand and A. N. Gent. Retention of liquid drops by solid surfaces. *J. Colloid. Interface Sci.*, 138:431–442, 1990.
 - [6] C. W. Extrand and Y. Kumagai. Liquid drops on an incline: The relation between contact angles, drop shape, and retentive force. *J. Colloid. Interface Sci.*, 170:515–521, 1995.
 - [7] B. Krasovitski and A. Marmur. Drops down the hill: Theoretical study of limiting contact angles and the hysteresis range on a tilted plate. *Langmuir*, 21:3881–3885, 2005.
 - [8] A. I. ElSherbini and A. M. Jacobi. Retention forces and contact angles for critical liquid drops on non-horizontal surfaces. *J. Colloid. Interface Sci.*, 299:841–849, 2006.
 - [9] N. Gao, F. Geyer, D. W. Pilat, S. Wooh, D. Vollmer, H.-J. Butt, and R. Berger. How drops start sliding over solid surfaces. *Nat. Phys.*, 14:191–196, 2018.
 - [10] N. Legrand, A. Daerr, and L. Limat. Shape and motion of drops sliding down an inclined plane. *J. Fluid Mech.*, 541:293–315, 2005.
 - [11] S. R. Annapragada, J. Y. Murthy, and S. V. Garimella. Prediction of droplet dynamics on an incline. *Int. J. Heat and Mass Transf.*, 55:1466–1474, 2012.
 - [12] F. Milinazzo and M. Shinbrot. A numerical study of a drop on a vertical wall. *J. Colloid. Interface Sci.*, 121:254–264, 1988.
 - [13] R. A. Brown, F. M. Orr, and L. Scriven. Static drop on an inclined plate: Analysis by the finite element method. *J. Colloid Interface Sci.*, 73:76, 1979.
 - [14] V. M. Starov and M. G. Velarde. Surface forces and wetting phenomena. *J. Phys.: Condens. Matter*, 21:464121, 2009.
 - [15] J. De Coninck, F. Dunlop, and T. Huillet. Contact angles of a drop pinned on an incline. *Phys. Rev. E*, 95:052805, 2017.
 - [16] A. I. ElSherbini and A. M. Jacobi. Liquid drops on vertical and inclined surfaces II. A method for approximating drop shapes. *J. Colloid. Interface Sci.*, 273:566–575, 2004.
 - [17] T.-H. Chou, S.-J. Hong, Y.-J. Sheng, and H.-K. Tsao. Drops sitting on a tilted plate: Receding and advancing pinning. *Langmuir*, 28:5158–5166, 2012.
 - [18] J. A. White, M. J. Santos, M. A. Rodriguez-Valverde, and S. Velasco. Numerical study of the most stable contact angle of drops on tilted surfaces. *Langmuir*, 31:5326–5332, 2015.
 - [19] B. Xu, Z. Yuan, and Y. Wu. Simulation analysis on surface morphology and hysteresis characteristics of molten Sn–3.0Ag–0.5Cu sitting on the inclined Ni substrate. *Colloids and Surfaces A*, 441:217–225, 2014.

- [20] A. K. Das and P. K. Das. Simulation of drop movement over an inclined surface using smoothed particle hydrodynamics. *Langmuir*, 25:11459–11466, 2009.
- [21] S. D. Iliev. Static drops on an inclined plane: Equilibrium modeling and numerical analysis. *J. Colloid Interface Sci.*, 194:287–300, 1997.
- [22] V. Berejnov and R. E. Thorne. Effect of transient pinning on stability of drops sitting on an inclined plane. *Phys. Rev. E*, 75:066308, 2007.
- [23] C.N.C. Lam, R. Wu, D. Li, M.L. Hair, and A.W. Neuman. Study of the advancing and receding contact angles: liquid sorption as a cause of contact angle hysteresis. *Adv. Colloid and Interface Sci.*, 96:169, 2002.
- [24] P. D. Ravazzoli, I. Cuellar, A. G. González, and J. A. Diez. Wetting and dewetting processes in the axial retraction of liquid filaments. *Phys. Rev. E*, 95:053111, 2017.
- [25] A. I. ElSherbini and A. M. Jacobi. Liquid drops on vertical and inclined surfaces i. An experimental study of drop geometry. *J. Colloid. Interface Sci.*, 273:556–565, 2004.
- [26] J. Diez, A. G. González, and L. Kondic. Instability of a transverse liquid rivulet on an inclined plane. *Phys. Fluids*, 24:032104, 2012.
- [27] P. D. Ravazzoli, A. G. González, and J. A. Diez. Drops with non-circular footprints. *Phys. Fluids*, 28:042104421, 2016.
- [28] P. Dimitrakopoulos and J. J. Higdon. On the gravitational displacement of three-dimensional fluid droplets from inclined solid surfaces. *J. Fluid Mech.*, 395:181–209, 1999.
- [29] A. G. González, J. Diez, R. Gratton, and J. Gomba. Rupture of a fluid strip under partial wetting conditions. *Europhys. Lett.*, 77:44001, 2007.